JOURNAL OF MAGNETIC RESONANCE **125,** 233–241 (1997)
ARTICLE NO. MN971136

A Method for Accurate Calculation of $\mathbf{B}_1$ Fields in Three Dimensions. Effects of Shield Geometry on Field Strength and Homogeneity in the Birdcage Coil

CHRISTOPHER M. COLLINS,*,† SHIZHE LI,† QING X. YANG,† AND MICHAEL B. SMITH†,‡

*Department of Bioengineering, University of Pennsylvania, Philadelphia, Pennsylvania 19104; and †Department of Radiology, Center for NMR Research, and ‡Department of Cellular and Molecular Physiology, Pennsylvania State University College of Medicine, Milton S. Hershey Medical Center, Hershey, Pennsylvania 17033

Received June 3, 1996; revised January 23, 1997

A method for calculating $\mathbf{B}_1$ field strength and homogeneity as functions of radiofrequency shield geometry is presented. The method requires use of three-dimensional finite-element analysis, birdcage-coil theory, and antenna-array theory. Calculations were performed for a 12-element birdcage coil (19 cm diameter, 21 cm length) at 125 MHz. Calculated $\mathbf{B}_1$ field strengths and homogeneities for the coil in 25 different shields and in no shield are given. For configurations where the shield is longer than the coil, both $\mathbf{B}_1$ field strength and homogeneity decrease as shield diameter decreases or as shield length increases. In configurations where the shield is shorter than the coil and has a diameter of 25.6 cm, $\mathbf{B}_1$ homogeneity is greater than in an unshielded coil. $\mathbf{B}_1$ field strength was measured experimentally at 125 MHz in a birdcage coil of the same geometry as the model within shields of four different diameters. Calculated results very closely matched experimental measurement.

INTRODUCTION

In the design of radiofrequency coils and shields, the effects of RF shield geometry are little understood and often ignored. Because RF shield geometry affects both RF magnetic-field ($\mathbf{B}_1$) strength and homogeneity, it is an important factor and should be considered. A homogeneous $\mathbf{B}_1$ field is necessary for production of good MR images (*1, 2*), and the signal-to-noise ratio available after a 90° pulse in systems where one coil is used to both transmit and receive is directly proportional to the $\mathbf{B}_1$ field strength in the homogeneous imaging region of the coil (*1*).

An RF shield serves to confine the region which is exposed to RF fields produced by the coil, shield the coil from RF fields produced elsewhere, and permit reproducible tuning of the coil in a variety of environments. In the development of working MR systems, space constraints place limitations on the size and shape of the RF shield. The shield must be large enough to accompany an RF coil appropriate for the study being done, and must fit within the magnet bore and gradient coils.

In order to construct an optimal RF system, it is important to consider how shield geometry will affect the performance of the RF system. It is possible to measure $\mathbf{B}_1$ field strength and homogeneity experimentally (*2, 3*). While this may at times be more practical than performing three-dimensional (3D) field calculations, experimental measurements of $\mathbf{B}_1$ field magnitude and homogeneity of RF systems require access to machining and electronics facilities, and specialized imaging sequences on an available MR system. Many researchers have found field calculation to be a desirable alternative to experimental measurement (*4–13*).

Much of the reason $\mathbf{B}_1$ field strength and homogeneity have not been accurately calculated as functions of shield geometry before now is due to the complexity of the problem. Complete consideration requires both thorough representation of currents and solution of the appropriate portions of Maxwell's equations in 3D. Two-dimensional calculations require much less computation than 3D calculations and have proven to be useful in a variety of coil-design applications (*4–6*), but they do not allow for complete, accurate simulation of shielded 3D coils. Several methods of calculation have been used to determine the magnetic fields produced by RF imaging coils in 3D (*7–13*). At this time, these methods either have not yet been applied successfully to solving optimization problems or have shortcomings that render them inadequate for thoroughly solving problems involving shielded coils in 3D. Ochi *et al.* have used the moment method of analysis to solve for the impedance of a birdcage coil (*7*). Their calculations of impedance as a function of frequency match experiment very well (*7, 14*), and the field plot they present looks reasonable (*7*). They have used their method to perform calculations of $\mathbf{B}_1$ strength as a function of shield length and diameter (*14*), but their calculations yield some counterintuitive results. They calculated that as shield diameter increases, the sensitivities of identical coils within shields of different lengths asymptotically approach different values, and the $\mathbf{B}_1$ strength in their

1090-7807/97 $25.00

calculations does not appear to approach zero as shield diameter decreases when shields are longer than the coil. (It is expected that $\mathbf{B}_1$ strength will approach the value for an unshielded coil as shield diameter approaches infinity for shields of any length, and that no field will be produced when the distance between the shield and the coil is zero as long as the shield is longer than the coil.) Zha *et al.* have presented a method using the Biot–Savart law and the method of images (*15*) to calculate the homogeneity of a multiple-element coil on a line along the *z* axis (*12*). While their method appears to yield reasonable results along this axis, it gives no information about the $\mathbf{B}_1$ field in the remainder of the coil.

By combining birdcage-coil theory, antenna-array theory, and a method of finite-element analysis that solves both the Biot–Savart law and Faraday's law simultaneously in 3D, we have calculated $\mathbf{B}_1$ field strength and homogeneity as functions of shield length and diameter in a birdcage coil. The results of this method are applicable at frequencies where one wavelength is much larger than the shield diameter. Because of our consideration of the entire coil in 3D and the agreement between calculation and experiment, the results presented here are more accurate and meaningful than those previously calculated for similar subjects (*12, 14*). We expect these results to be useful in the optimization of birdcage coil systems.

THEORY AND METHODS

Initial Calculations

In all calculations of field patterns and inductances, we employed Maxwell 3D Field Simulator software (Ansoft Corporation; Pittsburgh, Pennsylvania). This software uses finite-element analysis to solve the equations

$$\nabla \times \mathbf{B}/\mu = \mathrm{J} \qquad [1]$$

$$\nabla \times \mathrm{J} = -j\omega\sigma\mathbf{B} \qquad [2]$$

in the entire problem region for arbitrarily defined 3D material geometries and currents. Here, **B** is the magnetic flux density vector, **J** is the current density vector, j is the imaginary unit, ω is the radial frequency, μ is the material magnetic permeability, and σ is the material electrical conductivity. The Biot–Savart law (Eq. [1]) is equivalent to Maxwell's fourth equation without the displacement term. Faraday's law (Eq. [2]) is equivalent to Maxwell's third equation. Omitting the displacement term from the equations solved is a simplification that preserves computer memory by neglecting wavelength effects. The resulting method can only be applied to problems where wavelength effects are not expected. For purposes of MR, this includes whole-body clinical (64 MHz and less) systems, and most small-bore, high-field systems.

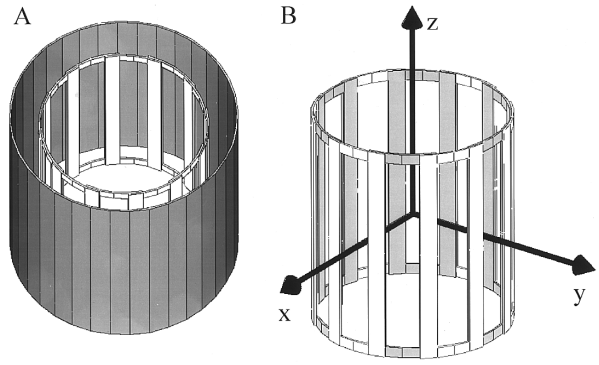

FIG. 1. Three-dimensional computer model of (A) the shielded 12-element birdcage coil, and (B) the coil having mesh loops in alternating shades (for ease of viewing) centered at the origin of a Cartesian coordinate system.

In solving problems with the finite-element method, the problem region is first divided into many subregions (in our case, tetrahedrons), varying in size as specified by the user. Then the equations of interest are solved simultaneously at the vertices of all the tetrahedrons with numerical methods for solving matrix equations. Once a solution is obtained, it is evaluated and the mesh of tetrahedrons is selectively refined so as to reduce the error, and the problem is solved again. This process of refining and solving is repeated until an acceptable solution is converged upon.

Although it is not possible to model capacitors with this software, we achieved the current pattern of the birdcage coil (Fig. 1A) in linear operation by modeling the birdcage as 12 separate loops placed with their centers at 30° increments around the perimeter of a circle in the axial plane with the legs of adjacent loops overlapping (Fig. 1B). Each loop was assigned a current magnitude proportional to the cosine of the angle between a line extending from the center of that loop to the center of the birdcage and the *y* axis (Fig. 1B). The current pattern produced with this method is consistent with birdcage coil theory for the entire coil as described in terms of mesh currents (*16*). The currents within the coil were assigned the same values regardless of shield geometry. All loops had a thickness of 2 mm and were assigned the material parameters of copper. Legs and end rings were 1.6 and 1.0 cm wide, respectively. The birdcage model was 19 cm in diameter and 21 cm in length.

Shields were modeled as thin cylindrical shells of perfect conducting material. Because the copper shields used experimentally were several skin depths thick, this is an acceptable method for modeling shields. Only the inner surface of a perfectly conducting shield model will have a noticeable effect on the field in the coil, so the thickness of the shield model will not affect the results. The finite thickness we chose to use in modeling shields was 2 mm. Sixteen shields were modeled, one for each combination of length and diameter for four lengths (1.14, 1.36, 1.70, and 2.00 times the

coil length) and four diameters (1.15, 1.35, 1.53, and 1.73 times the coil diameter). Nine additional shields were modeled, five with diameter 1.35 times that of the coil diameter and lengths 0.2, 0.4, 0.6, 0.8, and 1.0 times that of the coil length, and four to match the shields built for experimental measurement (described later) exactly in length and diameter. All models were centered in a problem region 2 m long in the z direction and 1 m long in each the x and y directions. The outer boundary of the problem region was constrained to have no field. Most problems were bisected by the $x-y$ plane with a perfectly conducting boundary on that plane before solution to conserve computer memory by taking advantage of this plane of symmetry and considering only half the original problem region. The final number of tetrahedrons per half-coil solution ranged from about 20,000 to about 54,000 with solutions having a larger region of interest (a larger shield), requiring a larger number of tetrahedrons. One solution of the magnetic field was obtained for the birdcage coil in each of the 25 shields and for the isolated birdcage. All calculations were performed on an IBM RISC 6000 Model 550 having 256 MB RAM. Time required per calculation varied from about 4 to about 14 hours, depending on the number of tetrahedrons.

Correction for Coil Impedance

The impedances within an actual coil are functions of the shield geometry. In practice, where coils are driven with controlled input voltages, the coil current magnitudes are thus functions of the shield geometry. Because, in our initial calculations, the coil current magnitudes were assigned the same values regardless of shield geometry, it was necessary to develop a method to account for the effect of impedance on the $\mathbf{B}_1$ field magnitude in order to achieve accurate predictions of experimental results. The necessary correction was made by first calculating the total impedance of one loop, then calculating the current in that loop as a function of the total impedance and the RF input voltage using Ohm's law. The correction for coil impedance was made for all of the calculations except for those where the shield was shorter than the coil.

When an RF current flows parallel to the surface of a shield, the effect of the shield can be effectively modeled by replacing the shield with an image of the current with flow in the opposite direction (*17*). In our correction of the initial finite-element calculations, we employ this method of modeling by considering the effect of the shield to be equivalent to the effect of images of all 12 loops of the coil with currents flowing in the opposite directions to those in the coil.

In theory, the total impedance of one loop is a function of its self-impedance, the mutual impedances between it and all the remaining loops, and the mutual impedances between it and the images of all the loops. In practice, we found it necessary to calculate the total impedance of one loop as a function of only its self-inductance, the mutual inductances between it and its four nearest neighboring loops, and the mutual inductances between it and the images of all five of these loops. This is consistent with findings by other investigators (*18, 19*). Because the resistive effects in each loop and the capacitive effects between loops are negligibly small, the total impedance of one loop can be calculated approximately as (*17*)

$$Z_0 = j\omega\Sigma(I_n L_{0,n})/I_0 + j\omega\Sigma(I_{n'} L_{0,n'})/I_{0'}, \qquad [3]$$

where the summation is performed over n, one n for each loop included in the calculation. Entities with primed subscripts are those of the image of loop n. Here Z_0 is the total impedance of loop 0, $L_{0,n}$ is the mutual inductance between loop 0 and loop n ($L_{0,0}$ is loop 0's self-inductance), and I_n is the current in loop n. Equations equivalent to this have been used to predict the resonant frequency shift of coils when placed in the presence of a shield (*18, 19*). We chose the loop with the greatest current, or the one centered on the y axis in the positive y direction to be loop 0. The position and current magnitude of each image were determined with the method of images (*15*). By this method, the image of an initial current is found so that the net field caused by the current and its image will have no component that is perpendicular to the surface of the shield at the shield/air interface, thereby satisfying boundary condition for an RF magnetic field at a perfectly conducting boundary. For a cylindrical shield, the distance from the center of the coil to the image of loop n ($R_{n'}$) can be estimated as

$$R_{n'} = (R_s)^2/R_c, \qquad [4]$$

where R_s is the radius of the shield and R_c is the radius of the coil. The current in the image of loop n, $I_{n'}$, in a cylindrical coil is equal in magnitude and opposite in direction to that in loop n.

All inductances were calculated with the Ansoft software. The mutual inductance between any two loops, $L_{m,n}$, was calculated by first solving for the $\mathbf{B}_1$ field created by each of the loops separately, then using the equation

$$L_{m,n} = (\mu I_m I_n)^{-1} \int \mathbf{B}_m \cdot \mathbf{B}_n dV, \qquad [5]$$

where I_m and I_n are the current magnitudes of the two loops, and $\mathbf{B}_m$ and $\mathbf{B}_n$ are the peak RF magnetic fields produced by each of the two loops. The integration was performed over the entire problem region. Each calculation of the mutual inductance between loop 0 and its own image was made with the equation

$$L_{0,0'} = \frac{L_{0,0} - (L_{0,0} + I_{0'}L_{0,0'})}{I_{0'}}, \quad [6]$$

where the first term in the numerator is the calculated self-inductance of loop 0 with no shield present, and the quantity in parentheses is the calculated self-inductance of loop 0 in the presence of the shield. Using the software, $L_{0,0}$ and $(L_{0,0} + I_{0'}L_{0,0'})$ were calculated separately. Each calculation of the mutual inductance between loop 0 and the image of a neighboring loop was made with the equation

$$L_{0,n'} = \frac{L_{0,0'}}{L_{0,0'}/L_{0,n'}}, \quad [7]$$

where the term in the denominator for each n' was calculated with the software after modeling the images of the loops for the case when the shield diameter was 1.17 times the coil diameter. It was assumed that these ratios of mutual inductances would not change significantly with shield diameter over the range of diameters used in our calculations.

The voltage differences both along end ring segments and along the legs in a coil form a sinusoidal standing wave around the *z* axis (*4, 20*). With direct (capacitive) feeding, either the maximum voltage drop across a segment of end ring (high pass coil) or the maximum voltage drop along one leg (low pass coil) is defined as the input voltage. The voltages in the rest of the birdcage must follow accordingly.

Now, from Ohm's law, assuming an identical input voltage, *V*, for each coil,

$$I_x/I_u = (V/Z_{0x})/(V/Z_{0u}) = Z_{0u}/Z_{0x}, \quad [8]$$

where x denotes values for any one-shielded model and u denotes values for the unshielded model. Because the $\mathbf{B}_1$ field magnitude, B_1, is directly proportional to the current strength,

$$B_{1x}/B_{1u} = (B_{1x,initial}/B_{1u,initial})(|Z_{0u}|/|Z_{0x}|), \quad [9]$$

where $B_{1x,initial}$ and $B_{1u,initial}$ are the magnetic field strengths from the initial calculations and B_{1x}/B_{1u} is the corrected ratio of the field strength of any one-shielded coil to that of the unshielded coil.

Calculation of B_1 Field Homogeneity

In quantifying the $\mathbf{B}_1$ field homogeneity of the 26 calculated field distributions, first the calculated $\mathbf{B}_1$ vector values at points spaced 3 mm apart in the *x*, *y*, and *z* directions within an 18-cm-diameter cylindrical sampling volume extending the length of the coil were extracted from each solution. From this vector information, the magnitude of the transverse (parallel to the *x*–*y* plane) component of the $\mathbf{B}_1$ field at each point was calculated. All points having magnitudes of the transverse component of the $\mathbf{B}_1$ field within ±10% of the value at the coil center were counted, and their number was divided by the total number of points in the entire sampling volume, yielding the fraction of the sampling volume that had a transverse component of $\mathbf{B}_1$ within ±10% of that at the center of the coil.

Experimental Protocol

In order to validate the accuracy with which our computational method can predict $\mathbf{B}_1$ field strength, we compared our computed results with experimental results for a birdcage coil shielded by four different diameter shields. Out of 0.127 mm thick copper tape, a 12-element high-pass birdcage coil with an inner diameter of 19 cm and a length of 21 cm was constructed on a cylindrical acrylic former. Legs and end rings were 1.6 and 1.0 cm wide, respectively. Four cylindrical copper shields with diameters of 22.4, 25.3, 29.1, and 32.9 cm, all 23.9 cm long, were constructed from 0.2 mm thick copper sheet. In each of the four shields, the coil was tuned to 125 MHz, driven with a voltage applied across one end ring capacitor, and the relationship between the $\mathbf{B}_1$ field strength at the center of the coil and the feed-point voltage was determined by each of two methods: (1) using a 2 cm diameter pick-up coil and a Hewlett–Packard 4195A network/spectrum analyzer to measure the $\mathbf{B}_1$ magnitude while driving with a known voltage, and (2) measuring the transmitting voltage required for a 180°, 50 μs, pulse on a 3 cm spherical sample of water placed at the coil's center in a 3.0 T, 90 cm bore Bruker MEDSPEC S-300 research MR imager. The accuracy with which finite-element calculations can be used to predict experimental field distributions has been demonstrated previously (*6*).

RESULTS

In Fig. 2, shaded plots of the calculated $\mathbf{B}_1$ field magnitude distribution for the case when shield diameter/coil diameter = 1.35 and shield length/coil length = 1.14 are shown on the (A) *x*–*y*, (C) *x*–*z*, and (E) *y*–*z* planes through the birdcage coil. To the right of the shaded magnitude plot for each plane is a vector plot showing the orientation of the field at different locations on the same plane (B, D, and F). This is the typical field pattern when current is maximum in a linear-field birdcage coil. For a rotating-field coil (i.e., a coil fed in quadrature), a similar field pattern will exist at any moment and will rotate about the *z* axis so that the time-average field magnitude will be nearly symmetric about the *z* axis. The field magnitude is most homogeneous at the center of the coil in the region with no contours, and least homogeneous close to the conductive elements, where there are several contours in close proximity. At the center of the coil, in the imaging region, the field orientation is also very uniform, as is seen in the vector plots. The arrows in the field

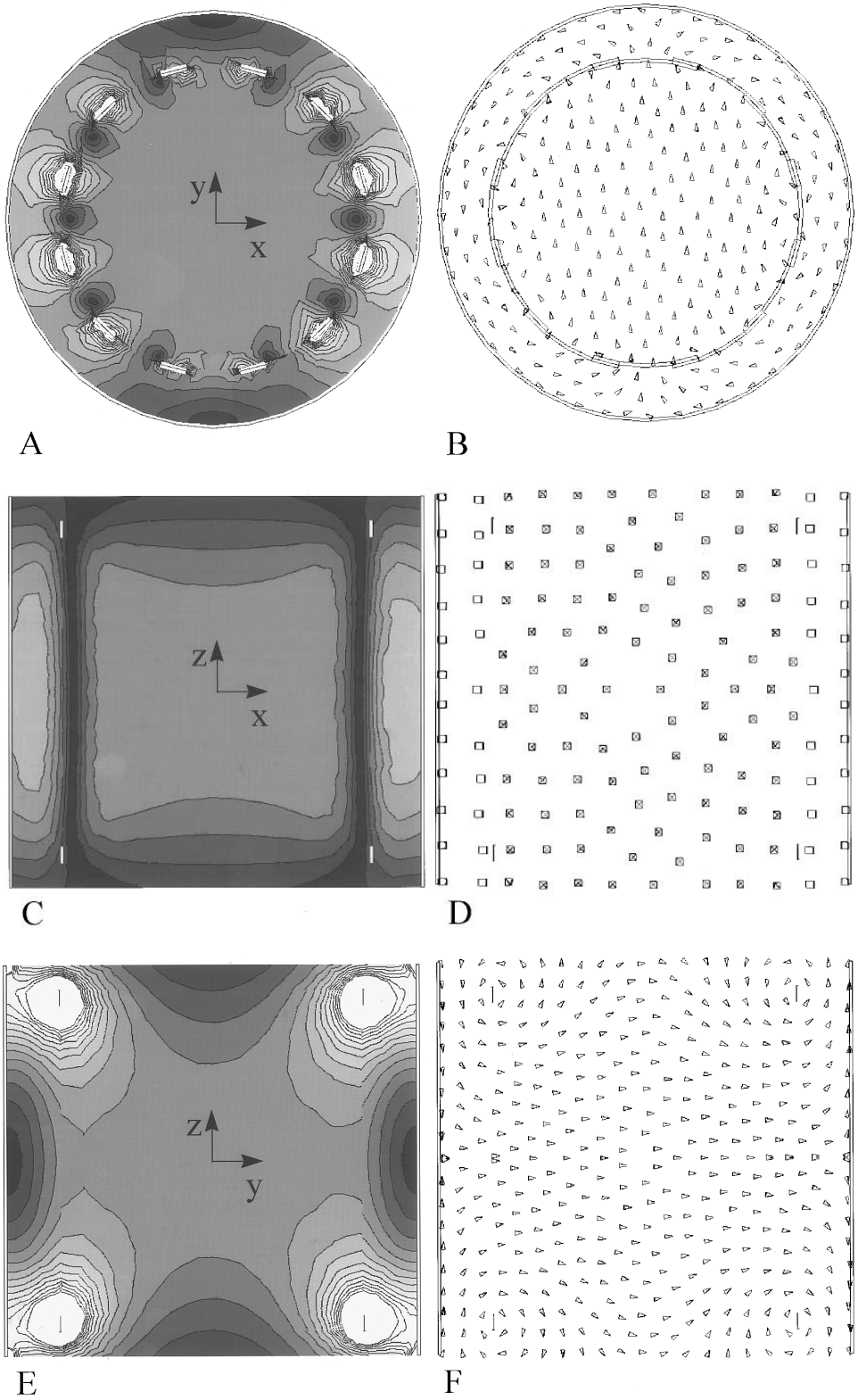

FIG. 2. Shaded magnitude plots and vector plots of $\mathbf{B}_1$ on the (A, B) x–y, (C, D) x–z, and (E, F) y–z planes. In the shaded plots, lighter shades cover regions of higher field magnitude plots. The contours separating two shades and that border the shade at the coil center mark ±10% deviation from the field magnitude at the coil center. Contours outside these mark deviations from the center magnitude of ±30%, ±50%, ±70%, etc. Shades and contour lines are plotted over a range from 10 to 310% of the center field magnitude. In vector plots, squares with Xs in them represent vectors pointing into the page, and empty squares represent vectors pointing out of the page.

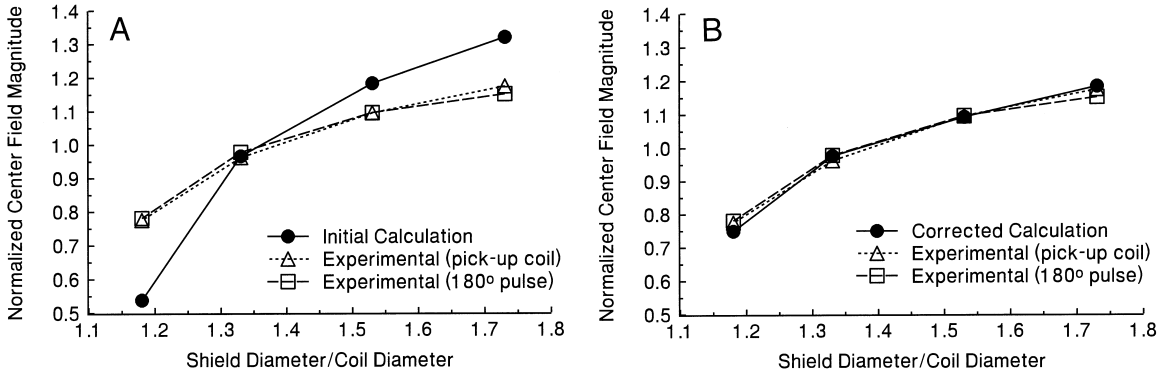

FIG. 3. Comparison of calculated and experimentally measured center-field magnitude before (A) and after (B) correction for coil impedance is made. Shield length is 1.14 times coil length. Field strength was measured experimentally both with a small pick-up coil and by measuring the transmitting power of a 180° pulse to a small sample of water. The magnitudes in each line have been normalized to the mean of all four values in that line.

vector plots curl around the current elements in a clockwise direction when the current in the element is flowing into the page and in a counterclockwise direction when the current in the element is flowing out of the page, in accordance with the Biot–Savart law and the right-hand rule convention. The current in the end rings is maximum where the current in the legs is minimum (near the y axis) because the currents from neighboring loops flow in opposite directions in the legs. The strongest magnetic field is in the y–z plane near the end ring, where the current in the birdcage coil has its absolute maximum.

In Fig. 3, calculated results are compared to experimental results to show that with our method of calculation, center field magnitude as a function of shield geometry can be calculated accurately for an actual birdcage coil that is driven with the same voltage magnitude and placed within different shields. In these plots, the data points in each line are normalized by the average of the four points in that line so that the calculated and experimentally measured values can be compared directly. The initial finite element calculation is not in good agreement with experiment, as shown in Fig. 3A. However, after the correction for coil impedance as a function of shield geometry is made, excellent agreement is achieved, as shown in Fig. 3B.

TABLE 1
Calculated Percent of Sampling Volume Having B_1 Strength within ±10% of Center B_1 Strength

D_s/D_c	L_s/L_c = 1.14	L_s/L_c = 1.36	L_s/L_c = 1.70	L_s/L_c = 2.00
1.15	38	37	36	36
1.35	44	43	42	41
1.53	45	44	43	43
1.73	45	44	44	44

Note. The value for the unshielded coil is 46. L is length, D is diameter, subscript s denotes shield values, and subscript c denotes coil values. Sampling volume fills 90% of the coil volume.

The values described as B_{1x}/B_{1u} in the methods section are plotted in Fig. 4. They are the calculated values for center field strength, corrected for impedance as a function of shield geometry and normalized to the field strength of an unshielded coil. As shown in Fig. 4, the center field strength of the birdcage coil is diminished as the diameter of the shield decreases and as the length of the shield increases. A point on the plot at (1.0, 0.0) could be added because, theoretically, when the distance between the coil and the shield is zero, no field is produced.

The calculated homogeneity of a birdcage coil with ideal currents as a function of shield geometry is tabulated in Table 1 for configurations where the shield is longer than the coil, and is plotted in Fig. 5 for configurations where the shield is shorter than the coil. Homogeneity is quantitated as the percent of the sampling volume having a component of magnetic field parallel to the axial plane within ±10% of that at the coil center. In cases where the shield is longer than the coil, homogeneity decreases with decreasing shield diameter and decreases very slightly with increasing shield length. In cases where shield diameter/coil diameter = 1.35, a maximum homogeneity is reached when the shield is about 0.6 times as long as the coil. At this maximum, about 3% more of the total sampling volume has a field magnitude within ±10% of that at the coil center than in the unshielded coil.

DISCUSSION AND CONCLUSIONS

The method presented here can be used to accurately calculate $\mathbf{B}_1$ field strength as a function of shield geometry in an empty birdcage coil. We have also previously shown that experimental field distributions can be calculated accurately with the finite-element method (*6*). Because Faraday's law is considered here, this method may also be used to perform accurate calculations for multiple-element and slotted-tube coils, whereas a method that uses only the Biot–Savart law

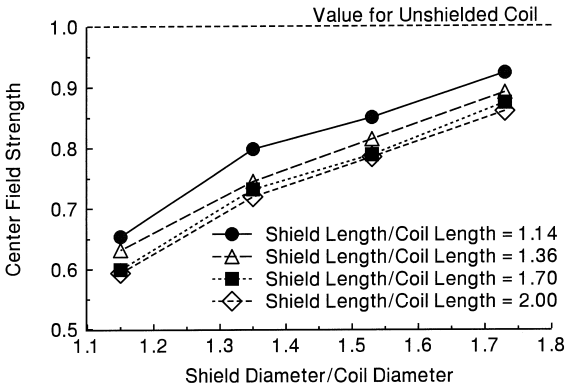

FIG. 4. Calculated values for center-field magnitude as a function of shield geometry for the coil within 16 different shields and for the unshielded coil. All magnitudes are normalized to the value for the unshielded coil. Calculations assume identical input voltage to the coil in all shield geometries.

can only calculate $\mathbf{B}_1$ field distributions when no eddy currents exist in the shield or coil (*5*) or when all currents are known *a priori.* Although it does not consider the dielectric term of Maxwell's equations, our method can be used to calculate magnetic fields that are not distorted by the presence of materials with high dielectric constants and that are at frequencies where the effective problem region (shield diameter) is much shorter than one wavelength in air. This includes all clinical and most small-bore high-field MR systems. Other methods with more thorough consideration of Maxwell's equations have been applied to solving for the electromagnetic fields in birdcage coils (*7–10*). When properly applied, these methods should give correct solutions at all frequencies for all coils. For calculations with the method presented here involving coils driven in quadrature, *V*, *I*, and *Z* in Eqs. [3], [6], and [8] must have complex values indicative of the magnitude and phase of each entity.

In this work, the coil diameter (19 cm) is small enough compared to one wavelength (240 cm in air at 125 MHz) that no significant wavelength effects are expected and all results can be discussed in terms of eddy currents and the Biot–Savart law. A time-varying magnetic field will induce an eddy current in a conductor such that the magnetic field produced by the induced current will oppose the original time-varying field. Therefore, the $\mathbf{B}_1$ field within a coil will be diminished by the presence of a conductive shield. It is not surprising that, as calculated with our method and shown in Fig. 5, the longer and closer to the coil the shield is, the more the field produced by the coil is diminished within the coil. This effect is not as dramatic as was predicted with our initial calculations (where current magnitudes in the birdcage were the same regardless of which shield was being used) because the overall impedance of the coil is reduced as the shield becomes longer and closer to the coil. This is because the contributing terms to total impedance that include mutual inductance between the coil elements and their images in the shield in Eq. [3] are negative since the currents in the images are in the opposite direction to those in the coil.

No results for field magnitude are given for cases where the shield is shorter than the coil. The calculations of homogeneity in these short shields were made to explore an interesting effect of homogeneity that was observed in previous calculations (*12*). It is doubtful that such short shields can shield effectively by themselves, and to examine whether using them in conjunction with other shields could be worthwhile would require further calculations. There is no reason to believe that the same trends calculated for long shields (i.e., decreasing field strength for decreasing shield diameter and increasing shield length) would not hold true for cases where the shield is shorter than the coil. Given the minimal calculated improvement in homogeneity seen by using short shields (an increase in homogeneous region of only 3% of the total coil volume), there may be little value in pursuing short shields as a means of homogenizing the RF field. In the presence of a second RF shield (to provide adequate shielding), gradient shields, and/or the magnet bore, the already minimal effect of the short shield would be damped.

Our calculations indicate that the overall homogeneity of the volume within a birdcage coil decreases as the shield decreases in diameter or increases in length in cases where the shield is longer than the coil (Table 1), and that a maximum homogeneity is reached for configurations when the shield is shorter than the coil (Fig. 5). It should be noted that the effect of shield geometry on field homogeneity is small compared to its effect on field magnitude, and compared to the effect that a tuning capacitor can have on homogeneity (*21*).

Examination of the $\mathbf{B}_1$ field throughout the coil in all shields revealed that shield geometry has two different effects on homogeneity, the first effect being dominant in long

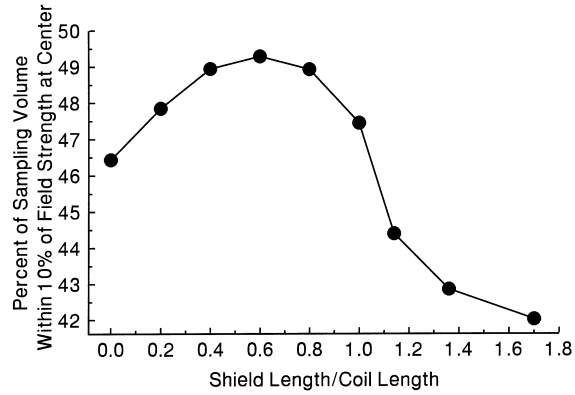

FIG. 5. Calculated values for percent of the sampling volume having a field magnitude within ±10% of that at the coil center as a function of shield length. Shield diameter/coil diameter = 1.35. Sampling volume fills 90% of the coil volume.

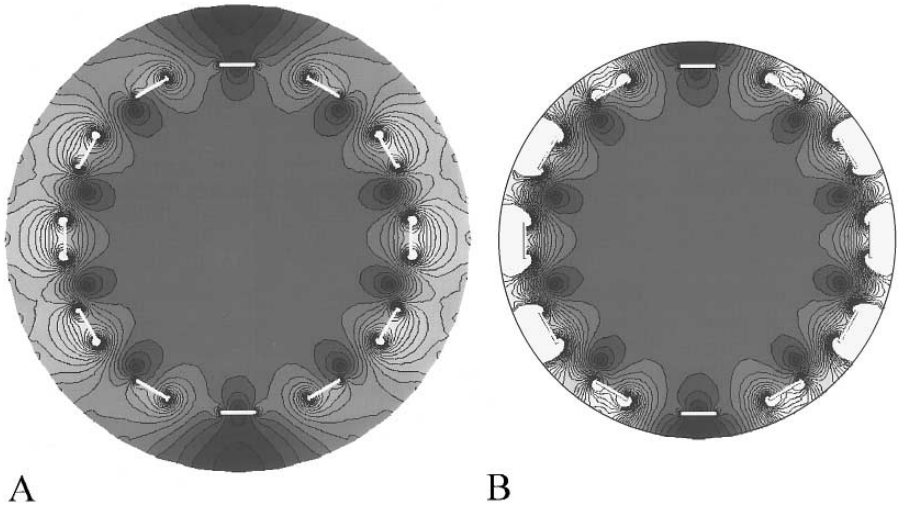

FIG. 6. Magnitude plots on the $x-y$ plane through coils with shield diameter/coil diameter equal to (A) 1.35 and (B) 1.15 made with 2D calculations. As the shield diameter decreases, the field strength between the coil and the shield becomes greater, resulting in a steeper radial field gradient near the edges of the coil and a smaller homogeneous region at the center of the coil. Shades and contours are as described in the legend to Fig. 2, plotted over a range from 10 to 510% of the center-field strength.

shields and the second being dominant in short shields. In cases where the shield was longer than the coil, there was little change in the homogeneity of a center cylinder 12 cm in diameter compared to the change in deviation from the center field strength in the remaining outer shell within the coil. The mechanism by which this occurs is illustrated in Fig. 6, which was produced with 2D finite-element software (*5, 6*). For illustrative purposes, the plots shown are equivalent to a plot on the $x-y$ plane through the center of a 3D coil. Figure 6A shows the calculated $\mathbf{B}_1$ field magnitude distribution for a shield diameter/coil diameter ratio of 1.35, and Fig. 6B shows the same for a ratio of 1.15. In both cases, the highest magnitude field is between the coil and the shield, but the field strength in this region is much higher than the field strength at the coil center in the case of the smaller shield. Using the right-hand rule and the Biot–Savart law, it is clear that the current in the images, which flows in the opposite direction to that in the coil elements, will produce a magnetic field between the coil and the shield which adds to the field produced by the current in the elements in this region, though it opposes the field produced by the current in the elements in the center of the coil. As

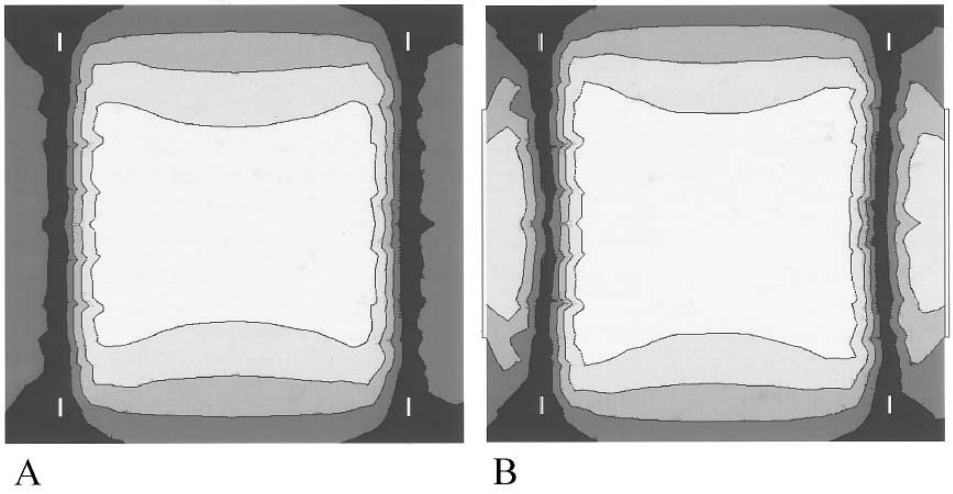

FIG. 7. Magnitude plots on the $x-z$ plane through coils with (A) no shield and (B) a shield 0.6 times the coil length and 1.35 times the coil diameter. The presence of the short shield weakens the field strength selectively at the center of the coil, making it more like the strength at the ends of the coil, and thus lengthening the homogeneous region. Shades and contours are as described in the legend to Fig. 2.

the shield decreases in diameter or increases in length, the field strength between the coil and the shield increases relative to that at the center of the coil, resulting in a greater $\mathbf{B}_1$ field magnitude gradient around the edges of the coil volume, and thus lower overall field homogeneity.

In cases where the shield was shorter than the coil, a different effect is predominant. This effect is illustrated in Fig. 7. Figure 7A shows the $\mathbf{B}_1$ field magnitude distribution on the $x-z$ plane of the unshielded coil, and Fig. 7B shows the same for the coil in a shield that is 0.6 times its length and 1.35 times its diameter. On this plane, the region with magnitude within $\pm 10\%$ of that at the coil center is noticeably longer for the case with the short shield. This is because the current induced in the shield creates a field that opposes the primary field selectively at the center of the coil, thus lowering the field magnitude at the coil center, making it more like the field toward the ends of the coil. The overall effect is to lengthen the region of homogeneity.

In this work, we have attempted to use the resources available to us to perform calculations that will be useful to a large portion of the MR community. As numerical methods of calculation become more accessible and computers at all levels become more powerful, similar calculations will be performed for a range of applications, yielding useful information about many different subjects. Two areas of interest are the behavior of high-frequency $\mathbf{B}_1$ fields in the human body and the currents induced in the body by rapidly switching gradient coils. We have demonstrated the accuracy of our methods for problems not involving the human body in this and previous publications (*5*, *6*). The general behavior of $\mathbf{B}_1$ field strength and homogeneity as functions of shield geometry presented here should be valid for birdcage coils over a range of sizes and frequencies, as long as the electromagnetic wavelength is much longer than the shield diameter. We hope that these results will be used in the design of RF coils in the future.

REFERENCES

1. D. J. Hoult and R. E. Richard, *J. Magn. Reson.* **24,** 71–85 (1976).
2. J. P. Hornak, J. Szumowski, and R. G. Bryant, *Magn. Reson. Med.* **6,** 158–163 (1988).
3. K. Beresten, S. M. Wright, and E. Boskamp, Abstracts of the Society of Magnetic Resonance, 2nd Annual Meeting, San Francisco, p. 1095, 1994.
4. C. E. Hayes, W. A. Edelstein, J. F. Schenck, O. M. Mueller, and M. Eash, *J. Magn. Reson.* **63,** 622–628 (1985).
5. S. Li, Q. X. Yang, and M. B. Smith, *Magn. Reson. Imag.* **12,** 1079–1087 (1994).
6. Q. X. Yang, S. Li, and M. B. Smith, *J. Magn. Reson. A* **108,** 1–8 (1994).
7. H. Ochi, E. Yamamoto, K. Sawaya, and S. Adachi, Abstracts of the Society of Magnetic Resonance in Medicine, 11th Annual Meeting, Berlin, p. 4021, 1992.
8. Q. X. Yang, H. Maramis, S. Li, and M. B. Smith, Abstracts of the Society of Magnetic Resonance, 2nd Annual Meeting, San Francisco, p. 1110, 1994.
9. J. H. McDuffie, J. G. Harrison, G. M. Pohost, and J. T. Vaughan, Abstracts of the Society of Magnetic Resonance, 3rd Scientific Meeting, Nice, p. 185, 1995.
10. Y. Han and S. M. Wright, Abstracts of the Society of Magnetic Resonance, 3rd Scientific Meeting, Nice, p. 1006, 1995.
11. C. Mahony, L. K. Forbes, S. Crozier, and D. M. Doddrell, *J. Magn. Reson. B* **107,** 145–151 (1995).
12. L. Zha, J. Lian, and I. J. Lowe, Abstracts of the Society of Magnetic Resonance, 2nd Annual Meeting, San Francisco, p. 1091, 1994.
13. E. C. Wong, A. Jesmnowicz, and J. S. Hyde, *Magn. Reson. Med.* **21,** 39–48 (1991).
14. H. Ochi, E. Yamamoto, K. Sawaya, and S. Adachi, Abstracts of the Society of Magnetic Resonance in Medicine, 12th Annual Meeting, New York, p. 1356, 1993.
15. P. M. Joseph and D. Lu, *IEEE Trans. Med. Imaging* **3,** 286–294 (1989).
16. J. Tropp, *J. Magn. Reson.* **82,** 51–62 (1989).
17. J. D. Kraus, ''Antennas,'' pp. 460–462, McGraw–Hill, New York, 1988.
18. R. Pascone, T. Vullo, J. Farrelly, and P. T. Cahill, *Magn. Reson. Imaging* **10,** 401–410 (1992).
19. J. Jin, G. Shen, and T. Perkins, Abstracts of the Society of Magnetic Resonance in Medicine, 12th Annual Meeting, New York, p. 1354, 1993.
20. R. J. Pascone, B. J. Garcia, T. M. Fitzgerald, T. Vullo, R. Zipgan, and P. T. Cahill, *Magn. Reson. Imaging* **9,** 395–408 (1991).
21. J. Jin, G. Shen, and T. Perkins, *Magn. Reson. Med.* **32,** 418–422 (1994).